

https://dspace.org/

Testing Primordial Black Hole Dark Matter with Atacama Large Millimeter Array Observations of the Gravitational Lens B1422231

Di Wen; Athol Kemball

https://hdl.handle.net/10539/40697
WOS

Downloaded from a DSpace repository. https://dspace.org/

universe

MDPI

Article

Testing Primordial Black Hole Dark Matter with Atacama Large Millimeter Array Observations of the Gravitational Lens B1422+231

Di Wen [1,2,*] and Athol J. Kemball [1,3]

[1] Department of Astronomy, University of Illinois at Urbana-Champaign, 1002 W. Green Street, Urbana, IL 61801, USA; akemball@illinois.edu
[2] Kapteyn Astronomical Institute, University of Groningen, P.O. Box 800, 9700AV Groningen, The Netherlands
[3] Wits Centre for Astrophysics, School of Physics, University of the Witwatersrand, P.O. Box Wits, Johannesburg 2050, South Africa
* Correspondence: wen@astro.rug.nl

Abstract: We examine the flux density ratio anomaly in the quadruply imaged strong gravitational lens, B1422+231, and consider the contribution of 10–$10^3 M_\odot$ primordial black holes (PBHs) as a potential dark matter constituent. We describe the first flux density ratio measurement of B1422+231 in the millimeter-wave band using the Atacama Large Millimeter Array (ALMA). The flux density of the quasar at 233 GHz is dominated by synchrotron emission and the source size is estimated to be less than 66.9 pc. The observed flux density ratios at 233 GHz are similar to those measured in other wave bands, which cannot be explained by a simple smooth mass model of the lens galaxy. We examine the probability of the flux density ratio anomaly arising from PBH microlensing using ray tracing simulations. The simulations consider the cases where 10% and 50% of dark matter are 10–$10^3 M_\odot$ PBHs with a power law mass function. The simulated scenarios are consistent with the ALMA observations, so PBH dark matter cannot be ruled out as a cause of flux density ratio anomalies. Our analysis shows that the anomalous flux density ratio for B1422+231 can be explained by a lens model with a significant fraction of dark matter being PBHs. This study demonstrates the potential for new constraints on PBH dark matter using ALMA observations of multiply imaged strong gravitational lenses.

Keywords: strong gravitational lensing; primordial black hole; cosmology; dark matter; quasars

check for updates

Citation: Wen, D.; Kemball, A.J. Testing Primordial Black Hole Dark Matter with Atacama Large Millimeter Array Observations of the Gravitational Lens B1422+231. *Universe* **2024**, *10*, 37. https://doi.org/10.3390/universe10010037

Academic Editor: Gonzalo J. Olmo

Received: 30 November 2023
Revised: 28 December 2023
Accepted: 8 January 2024
Published: 12 January 2024

Copyright: © 2024 by the authors. Licensee MDPI, Basel, Switzerland. This article is an open access article distributed under the terms and conditions of the Creative Commons Attribution (CC BY) license (https://creativecommons.org/licenses/by/4.0/).

1. Introduction

The nature of dark matter remains as a puzzle. It is plausible that a fraction of the dark matter in galaxies and their surrounding dark matter halos could come from primordial black holes (PBHs). The idea that a fraction of dark matter could be PBHs in the mass range 10–$10^3 M_\odot$ has become more popular (e.g., [1,2]) after the gravitational wave detections of merging binary black holes with masses above $10 M_\odot$ [3,4]. Observational constraints on the fraction of dark matter in a wide range of compact object masses show that PBHs of mass 1–$10^3 M_\odot$ might be a candidate for dark matter [2]. The mass and abundance of PBH dark matter are constrained by microlensing [5,6], star clusters [5,7], dwarf galaxies [8,9], and wide binary stars [10,11]. Recently, there has been strong observational evidence for a 150 $M_\odot$ intermediate-mass black hole (IMBH), the remnant of a binary black hole merger [12]. Such IMBHs could also be PBHs. At the highest accuracy, constraints on the fraction of dark matter as PBHs have to be calculated based on an extended PBH mass function. PBHs with a unified multi-modal mass function that peaks at around 10^{-5}, 2, 30 and $10^6 M_\odot$ could provide the dark matter and satisfy a variety of observational constraints [13,14]. A recently proposed method calculates the allowed mass range of primordial black holes as dark matter based on published constraints for the black hole mass

function [2]. In particular, bounds from microlensing and accretion show 10–$10^3 M_\odot$ PBHs can constitute a fraction or all of dark matter [13,15]. Unfortunately, the mechanism for forming IMBHs, either from massive stars or primordial black holes, is not well understood (see [16] for a review).

Gravitational lensing provides some of the most compelling and direct evidence for dark matter (e.g., [17]). General relativity predicts that light rays are deflected by massive objects. The deflection of light due to a gravitational lens galaxy or galaxy cluster can distort the shapes of the source galaxy images in the case of weak gravitational lensing, or produce multiple distorted images of the source galaxy in the case of strong gravitational lensing [18,19]. Furthermore, different mass distribution in the gravitational lens produce different image positions, shapes and flux densities. This makes gravitational lensing one of the most powerful tools for probing the distribution of dark matter.

Numerical simulations have shown that in the cold dark matter paradigm, hierarchical structure formation produces a large population of dark matter substructures (DMSs) within galaxy-sized and cluster-sized dark matter halos [20,21]. The DMSs should potentially host dwarf galaxies or satellite galaxies, but the observed abundance of dwarf galaxies does not agree with the predicted abundance of DMSs [22,23]. This 'missing satellite problem' has recently been resolved by taking observational selection function into account [24]. The distribution of dark matter in dark matter halos is clumpy because of the presence of DMSs. Their signatures on the lensed images make galaxy–galaxy strong gravitational lenses the best targets for detecting DMSs observationally. Several techniques have been developed for detecting individual DMS [25–30], measuring the DMS power spectrum [31,32], and extracting the halo mass function [33,34] with strong gravitational lensing. DMSs near a strongly lensed image, either inside the lens galaxy halo or along the line of sight, perturb the smooth gravitational potential of the lens halo and change the magnification and the flux densities of lensed images [35–39]. This leads to anomalous flux density ratios that cannot be explained by a smooth lens. The presence of DMSs affects the flux density ratios observed in all wave bands.

DMSs may not be the only dark perturbers causing flux density ratio anomalies. A population of PBHs as a fraction of dark matter could be another non-smooth mass component of the lens galaxy. Compact perturbers with masses 10–$10^5 M_\odot$ are considered IMBHs, which can be of primordial origins. A stellar component on top of smoothly distributed dark matter in the lensing galaxy has been shown to enhance microlensing fluctuations and broadens the magnification probability distribution toward both magnification and demagnification [40,41]. The flux density ratio anomalies observed in optical and X-ray bands are usually caused by stellar microlensing. Similarly, microlensing by a population of IMBHs can produce additional magnification on top of a macro-lensed image, producing an uneven magnification distribution. The distortion pattern of an individual IMBH along the line of sight in the lensing galaxy has an angular scale of a few μas to mas [42], equivalent to the Einstein radius of a point mass IMBH at a typical lens redshift. Even though individual microlens' Einstein radius is much smaller than the source size, the net magnification due to microlensing by a population of stars converges to a constant low magnification for large source sizes, shown by Barvainis and Ivison [43] for 30 lensed quasars at submillimeter bands. A population of IMBHs can in principle produce analogous effects and have a significant contribution to the mm-wave flux density ratio anomaly. IMBHs could also be the answer to the issue raised by Xu et al. [44] that DMSs are unlikely to be the full reason for lensed flux density ratio anomalies in the radio band. Schechter et al. [41] demonstrated using microlensing simulations that the magnification probability distribution depends on the mass spectrum of the compact objects. Assuming a fraction of dark matter is PBHs, a strongly lensed quasar could show flux density ratio anomalies caused by quasar microlensing where PBHs act as microlenses. The degree of flux density ratio anomaly observed in a multiply imaged, strong gravitational lens system could place new constraints on PBH dark matter.

In this study, we examine the plausibility of the flux density ratio anomaly arising from PBH microlensing. The fraction of PBH dark matter between 10^4–$10^6 M_\odot$ has recently been

constrained to be less than 0.17 with 11 quadruply lensed quasars using an approximate Bayesian computation forward modeling technique [45]. In our complementary study, we focus on PBHs in the low mass range of IMBHs, 10–$10^3 M_\odot$ and use frequentist statistics to quantify if PBH dark matter alone, without the addition of DMSs, is consistent with the observed flux density ratios of a quadruple lens system with known flux density ratio anomalies. Using one lens system as an example, we provide motivation for more mm-wave observations of a sample of quadruple lens systems in the future to constrain the PBH dark matter fraction and the IMBH mass function in the low-mass range.

In this paper, Section 2 describes the first flux density ratio measurement in the mm-wave band for the strong gravitational lens, B1422+231. Section 3 presents the lens and source models for the ALMA observations. In Sections 4 and 5, we examine whether PBHs alone can produce the quadruply lensed flux density ratio anomalies by performing PBH microlensing simulations.

2. ALMA Observations of B1422+231

B1422+231 is a quadruply lensed radio-loud quasar that is known for its flux density ratio anomaly. It has previously been observed in radio, infrared, optical and X-ray wave bands. We observed B1422+231 for the first time in the mm-wave band with ALMA. Continuum observations in Band 6 at 233 GHz over a total bandwidth of 7.5 GHz were carried out in two execution blocks on 2019 June 19 and 27 with ALMA using a hybrid configuration of C43-9 and C43-10 (Project ID: 2018.1.00915.S). The ALMA array consisted of 43 long baseline antennas and baseline lengths ranged from 83.1 m to 16.2 km. The calibrators were J1256-0547, J1427+2348 and J1436+2321. The total on-source integration time was 69.02 min. The data collected in the first execution block passed quality-assurance stage 0 and 2. The data collected in the second execution block were classified "SemiPass" in quality-assurance stage 0 due to bad phase transfer from the phase calibrator to the target. The Common Astronomy Software Applications package (CASA; [46]) and ALMA pipeline (Version 6.2.1.7; Pipeline Version 2021.2.0.128) were used for calibration and imaging for data from both execution blocks. The measurement set from each execution block was calibrated separately, first with the ALMA pipeline and then phase self-calibrated. The phase self-calibration used a 80 s solution interval for the first execution block and a 70 s solution interval for the second execution block. The image signal-to-noise (S/N) for the second execution block is 2.3 times lower than that of the first execution block, due to the large noise in phase. Amplitude and phase calibration were performed after combining the two phase self-calibrated measurement sets in order to align the flux scales measured on two observation dates, assuming the source was not variable. To improve sensitivity to the weakest demagnified lensed image, imaging was carried out using natural weighting of the visibilities. Figure 1 shows the final image of the self-calibrated combined measurement sets.

The total continuum flux density of B1422+231 at 233 GHz we measure is 6.305 ± 0.082 mJy, summing the flux densities from all four lensed images. This is slightly lower than the measured flux density of 7.5 ± 0.8 mJy at 238 GHz by the Submillimeter Array [47]. The missing flux density is likely caused by the fact that our maximum recoverable scale (MRS) is smaller than the extended emission along the lensing arcs near the image triplet (see Section 3.2). An MRS of $0.322''$ is derived for the hybrid ALMA configuration, based on the fifth percentile baseline length 810.7 m. The angular sizes of the arcs are expected to be comparable to the image separations ($\sim 0.50''$ between image A and B and $\sim 0.82''$ between image B and C). The delivered data were incomplete relative to our proposal request due to a proposal scheduling priority. We requested hybrid observations including the more compact C43-6 configuration, but no data were taken with this configuration. Assuming the radio synchrotron spectral index -1.35 derived from measurements at 15.0 and 22.5 GHz [48,49], we expect a flux density of 6.13 mJy at 233 GHz and 5.96 mJy at 238 GHz. Our measured flux density is consistent with these values, suggesting the detected compact emission at in Band 6 is mostly dominated by the synchrotron emission

from the quasar's active galactic nucleus (AGN) with almost no thermal dust emission from the dusty torus expected to surround the accretion disk [50].

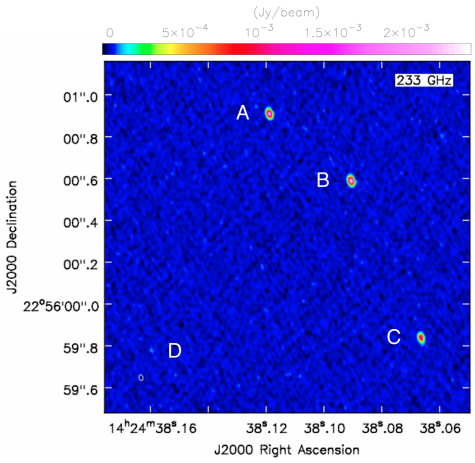


Figure 1. Naturally weighted ALMA Band 6 continuum map of B1422+231 at 233 GHz over a 7.5 GHz total bandwidth. The size of the restoring beam is $0.045'' \times 0.022''$, shown in the bottom-left corner. The rms noise level is 11 μJy beam^{-1}. Four unresolved point sources are detected and labeled as images A, B, C, and D.

Flux Density Ratio of Image Components

Image A, B, and C correspond to the brightest three image components in a cusp configuration of the quadruply imaged B1422+231 (see Figure 1). The foreground lens galaxy is not detected, which is expected at this frequency. Image A, B, and C are individually fitted with two-dimensional elliptical Gaussian image components parametrized by peak intensity, peak pixel coordinates, major and minor axes, and position angle using CASA. The best-fit image properties are presented in Table 1. The image positions in our observation are consistent with those from radio, infrared and optical observations [29,51–53]. The apparent alignment of position angles among A, B, and C in Figure 1 only reflects the position angle of the beam, which has higher angular resolution along the tangential direction of the triplet's arc than the radial direction. The uncertainties of the fitted position angles for the three image components after devolution from the beam (in the last column of Table 1) are likely underestimated. The error estimates of the integrated flux to image components are calculated during the Gaussian fitting implemented in CASA. The error estimates to the fitting parameters are based on the formulation by Condon [54]. The image component positions from Gaussian fitting before self-calibration are the same as those in Table 1. Image component D has the largest position uncertainties from Gaussian fitting due to its low S/N, 1.3 mas in right ascension, and 2.6 mas in declination. Figure 2 shows the flux density ratio of B1422+231 measured across the electromagnetic spectrum. We find that the flux density ratio (A+C)/B for B1422+231 at 233 GHz to be 1.434 ± 0.017, consistent with the values from radio, mid-infrared and most optical observations. The frequency-independent flux density ratios in radio, mm and mid-infrared observations suggest that the emissions at these frequencies likely originate close to the accretion disk of the AGN. Most flux density ratios across all frequencies in Figure 2 deviate significantly from the prediction from the best smooth lens model by Xu et al. [44], which indicates that the mass distribution in the foreground lens galaxy is not smooth. The presence of DMSs is likely the primary contributor to the observed flux density ratio anomalies at low frequencies. The large scatter and deviation from the smooth model prediction in optical and X-ray observations suggests that stellar microlensing likely causes additional flux density ratio anomaly contributions.

Table 1. B1422+231 image positions and flux densities measured in ALMA Band 6 continuum observations. The major axis and the minor axis are the FWHM of the best-fit 2-dimensional Gaussian image component sizes after deconvolution from a $0.045'' \times 0.022''$ restoring beam with position angle 24.756°. The phase center coordinates are J2000 RA 14:24:38.1168, Dec +22:56:00.175.

Image	Right Ascen. (h m s)	Declination (° ′ ″)	$\Delta\alpha\,cos(\delta)$ (arcsec)	$\Delta\delta$ (arcsec)	Flux Density (mJy)	Flux Density Ratio	Major Axis (mas)	Minor Axis (mas)	PA (deg)
A	14:24:38.118	+22:56:00.890	+0.017	+0.715	2.338 ± 0.019	0.912 ± 0.011	5.87 ± 0.97	2.62 ± 1.48	35 ± 14
B	14:24:38.090	+22:56:00.570	−0.370	+0.395	2.565 ± 0.023	1	8.53 ± 0.70	0.76 ± 1.25	23.9 ± 4.3
C	14:24:38.066	+22:55:59.823	−0.702	−0.355	1.339 ± 0.022	0.522 ± 0.010	7.8 ± 1.3	1.2 ± 1.3	16.5 ± 8.7
D	14:24:38.158	+22:55:59.762	+0.569	−0.415	0.063 ± 0.018	0.025 ± 0.007	-	-	-

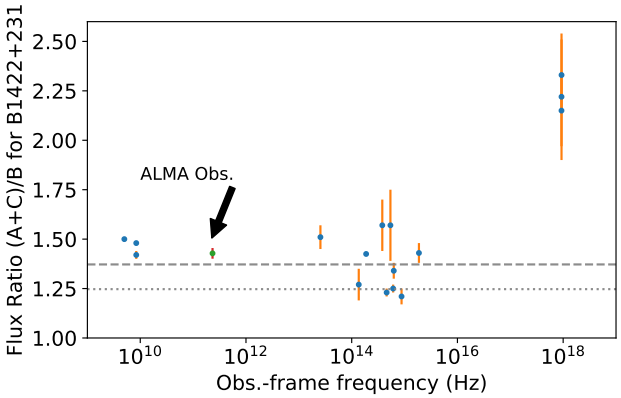


Figure 2. Flux density ratio anomalies as a function of observing frequency [51–53,55–57]. The orange error bars of flux density ratios are calculated from the individual lensed image flux densities and associated error bars reported in the literature, following the standard propagation of uncertainties. Our ALMA Band 6 observation labeled with an arrow shows a flux density ratio of (A+C)/B = 1.434 ± 0.017, consistent with measurements in radio and mid-infrared frequencies. The dotted and dashed horizontal lines show the predictions of the best-fit smooth lens model by Xu et al. [44], (A+C)/B = 1.247 and by Schechter et al. [58], (A+C)/B = 1.372. Data points with large deviation from the horizontal lines exhibit large flux density ratio anomalies.

3. Lens and Source Model of B1422+231

The starting point of our mass model for B1422+231 is a singular isothermal ellipsoid (SIE) plus external shear γ_x (SIE+γ_x) model. Optical and near-infrared observations have shown that B1422+231 belongs to a group consisting of five nearby galaxies that provide sufficient external shear to produce the observed image configuration [59]. The source galaxy is at redshift $z_s = 3.62$ and the foreground lens galaxy is at redshift $z_l = 0.34$ [51,60]. We modeled the ALMA observation of B1422+231 in three steps: (1) lens modeling with image positions and/or flux densities as constraints assuming a point source; (2) visibility-space parametric source modeling while holding the lens model fixed; and (3) visibility space joint parametric modeling of the lens and source. A Hubble constant $H_0 = 67.7$ km Mpc^{-1} s^{-1} and a matter density parameter $\Omega_M = 0.307$ [61] are assumed.

3.1. Lens Model

We first used only the image positions in Table 1 as constraints and modeled the lens system with the software package `glafic` (version 2; [62]), which minimizes χ^2 in the source plane. The SIE+γ_x model includes seven parameters (columns 4–10 in Table 2): relative positions of the dark matter halo center to the phase center in RA and DEC directions Δx_l and Δy_l, Einstein radius θ_{Ein}, ellipticity of the lens halo e, position angle of the lens dark matter halo θ_e, external shear γ_x and position angle of the external shear θ_x. The source model is a point source with coordinates Δx_s and Δx_y relative to the phase center. We show the best-fit lens model with both the image positions and flux densities as constraints. However, because of the known flux density ratio anomaly of this system, the best-fit lens

model using only image position as constraints is more reliable than that with flux densities as constraints. Table 2 shows that our model with only position constraints is similar to the published model obtained for [O III] images using only image positions as constraints [29].

Table 2. Best-fit lens model parameters. The first two lines are fitted using `glafic`. Note that Δx_s and Δx_l have opposite signs compared to $\Delta\alpha\, cos(\delta)$ in Table 1. The position angle θ_e is defined in degrees east of north in `glafic`, where +x direction is west and +y direction is north. The SIE ($\bar{S}_\nu$) model uses only image component positions as constraints and not flux densities. The SIE (S_ν) model uses both image component positions and flux densities as constraints. A SIE ([O III]) model from Nierenberg et al. [29] is included for comparison.

Model	Δx_s (arcsec)	Δy_s (arcsec)	Δx_l (arcsec)	Δy_l (arcsec)	θ_{Ein} (arcsec)	e	θ_e (deg)	γ_x	θ_x (deg)
SIE ($\bar{S}_\nu$)	−0.071	−0.070	−0.355	−0.264	0.7755	0.285	127.3	0.172	125.0
SIE (S_ν)	−0.066	−0.068	−0.423	−0.310	0.7996	0.477	126.6	0.117	125.0
SIE ([OIII])	-	-	−0.3896	−0.2404	0.771	0.16	123	0.22	126

3.2. Source Model

Secondly, we reconstructed the source by holding the 'SIE ($\bar{S}_\nu$)' lens model fixed and fitting a Sérsic profile using the software package `visilens` [63,64], a Python package for modeling interferometric observations of strong gravitational lensing systems. The source emission was modeled with a Sérsic profile [65] with seven parameters (columns 2–8 in Table 3; Figure 3): relative position of the source center to the lens center in the RA and DEC directions ΔX_s and ΔY_s, total integrated flux density of the source F_s, source major axis a_s, Sérsic profile index n_s, source minor to major axis ratio b_s/a_s and source position angle ϕ_s. The software `visilens` was modified to make use of the importance nested sampling algorithm `Multinest` [66–68] and its Python interface `PyMultiNest` [69] for improved fitting efficiency and more precise estimation of the parameter uncertainties for the best-fit model in a multi-model parameter space. The calculation of the log-likelihood function in `visilens` remains unchanged. A constant efficiency mode of `MultiNest` with a sampling efficiency of 0.1 and 1000 live points was used. To reduce the number of visibilities to model, the continuum visibility data were averaged over 128 frequency channels in each spectral window spanning 1.875 GHz and 6.048 s in time. This is a prudent choice because the response R_a to a point source resulting from this averaging is close to 1 (Equation (6.80) in [70]). In comparison, the source model assuming the 'SIE ($\bar{S}_\nu$)' lens model has higher log-evidence log Z than that assuming the 'SIE ([O III])' lens model in the last column of Table 3.

The model image from our best lens and source model 'SIE ($\bar{S}_\nu$)' is shown in Figure 4. All four image positions can be reproduced. Our model predicts an intrinsic source flux density of 0.2963 μJy and total magnification of 24.22, corresponding a total flux density of 7.176 mJy after lensing. The model-predicted extended arcs near the triplet images were not observed, due to the low sensitivity of the hybrid array to the angular scales of these arcs discussed in Section 2, resulting in a lower total observed flux density of 6.305 mJy. The model predicted Sérsic source major axis of 9.03 mas corresponds to 66.9 pc at the redshift of this source. This physical size is similar to the narrow-line [O III] size of 60 pc [29]. The true source size may be smaller than the size of our fitted Sérsic profile, because the source structure is not well resolved by this observation. It is possible that our model predicts a more extended source than the true source and hence produces the extended arcs in the model image. Observations with a more compact ALMA configuration that are more sensitive to the source extended emission can better image the lensing arcs, if any. The fitted Sérsic index n_s much smaller than 0.5 describes a sharp cutoff to the source surface profile. This is likely because the synchrotron emission of source does not resemble the Sérsic profile.

Table 3. Best-fit Sérsic source model parameters using `visilens`. The source position angle ϕ_s is defined in degrees counter-clockwise from the lens major axis (see Figure 4), where +x direction is west and +y direction is north. The last column lists the relative log-evidence. The SIE ([O III]) model assumes the lens model in Table 2 [29].

Lens Model	ΔX_s (arcsec)	ΔY_s (arcsec)	F_s (μJy)	a_s (mas)	n_s	b_s/a_s	ϕ_s (deg)	$\Delta\log Z$
SIE ($\bar{S}_\nu$)	$0.34436^{+0.00052}_{-0.00073}$	$0.23053^{+0.00025}_{-0.00037}$	$0.2963^{+0.0043}_{-0.0038}$	$9.03^{+0.15}_{-0.12}$	$0.050^{+0.011}_{-0.015}$	$0.850^{+0.024}_{-0.026}$	105^{+20}_{-10}	0
SIE ([O III])	$0.36007^{+0.00093}_{-0.00025}$	$0.24717^{+0.00063}_{-0.00070}$	$0.97^{+0.77}_{-0.71}$	$9.07^{+1.10}_{-0.96}$	$0.106^{+0.057}_{-0.058}$	$0.166^{+0.066}_{-0.034}$	$72.88^{+0.56}_{-1.0}$	-2589

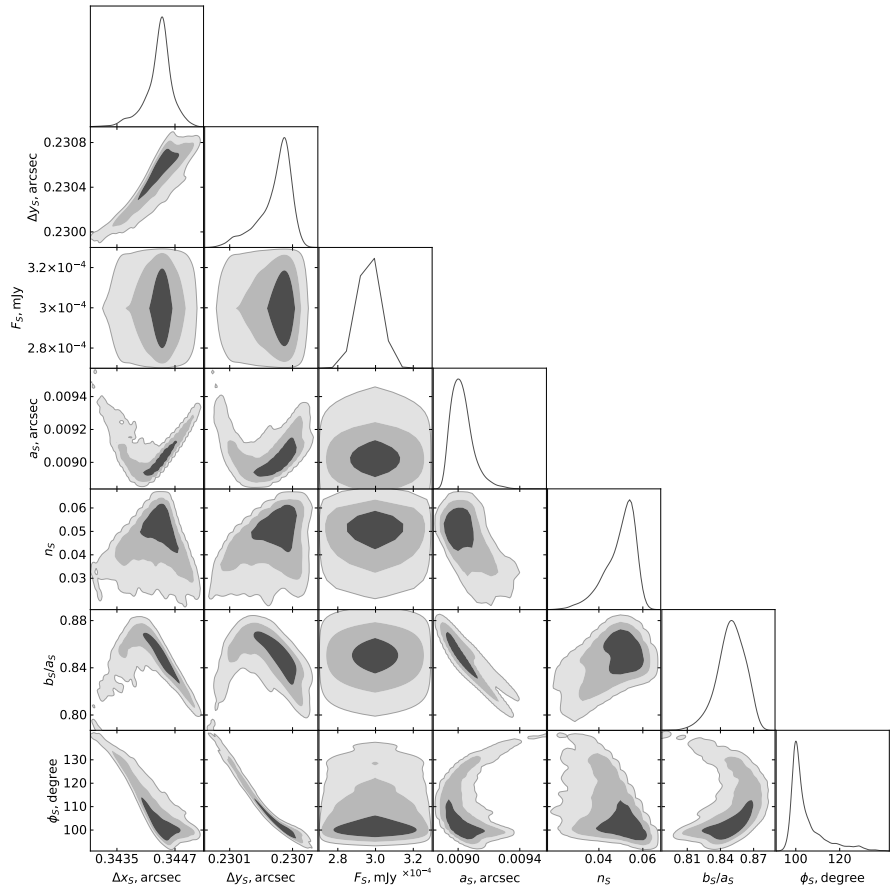


Figure 3. Source parameter degeneracy assuming the SIE ($\bar{S}_\nu$) lens model. The contours show the 68%. 95%, and 98% confidence regions.

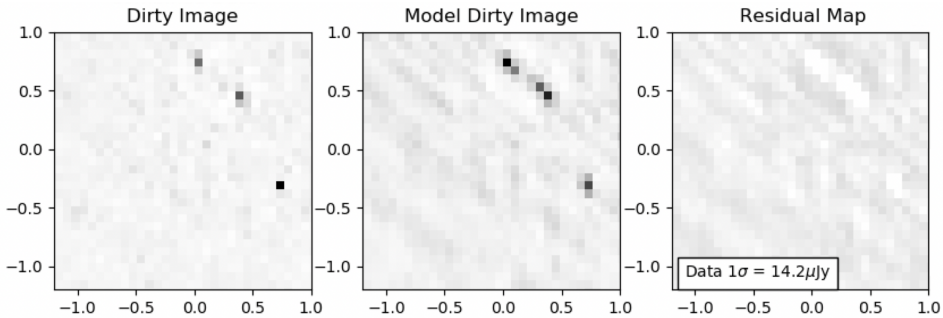


Figure 4. (**Left**): B1422+231 dirty image based on the calibrated ALMA Band 6 visibility data. (**Middle**): model dirty image based on the simulated visibilities for the best-fit SIE ($\bar{S}_\nu$) lens model and Sérsic source profile. (**Right**): residual map with an estimated noise level. The coordinates are in units of arsecs centered at the phase center in Table 1.

3.3. Joint Modeling

Thirdly, we attempted modeling the visibility data directly by jointly fitting fourteen model parameters for the lens, external shear, and a Sérsic source using both the original version of `visilens` and our modified `visilens` with the `MultiNest` sampler. The best-fit model image produced by the original `visilens` could not reproduce the relative image positions. The fitted image positions were more widely separated than those in the observation. The poor fits were caused by the low S/N of image D in the visibility data, resulting in large uncertainties in lens mass, lens position, and source position. Large uncertainties for the source model parameters are also expected, given the under-constrained lens model and unresolved source. Jointly fitting the lens, external shear, and the source using the modified `visilens` with `MultiNest` sampler did not converge to produce a best-fit model. Therefore, we conclude that the joint lens and source model cannot be well constrained by the current data.

The failure of a smooth mass model is not surprising for this source. B1422+231 has been chosen for this study because of its known flux density ratio anomaly. Modeling visibilities directly makes use of both the position and flux density information of the image components. For a system with a flux density ratio anomaly, the best-fit smooth lens model constrained by the image component flux density information is bound to be inaccurate by design. Therefore, lens modeling for systems with flux density ratio anomalies are usually only based on the positions of image components. Previous work has shown that the best-fit SIE+γ_x models with and without B1422+231 image flux densities are noticeably different [29]. Previous SIE+γ_x models for B1422+231 observed in other frequencies can mostly reproduce the image component positions, but they also have difficulties matching the observed component flux densities [29,58,71–73]. Their best-fit SIE+γ_x model parameters can sometimes differ significantly because of the uncertainties in image component positions and flux densities in different frequency bands. The positions of image components are very sensitive to the source and lens positions, in particular, the relative position of the source to the caustics. The S/N of the image components in the dirty image is too low for visually identifying the image component. The `visilens` software optimizes χ^2 for model visibilities and marginalizes over phase errors instead of optimizing the fit to image component positions. The constraints from image component positions cannot be disentangled from the constraints from image component flux densities. This makes modeling visibilities directly for a lens system with anomalous flux density ratios challenging.

4. Primordial Black Hole Microlensing Simulation

If a fraction of dark matter is in PBHs, microlensing by a population of PBHs creates a scatter in lensing magnifications of strongly lensed images. We perform PBH microlensing simulations to quantify the effects of PBH dark matter on image component flux density ratios. The brute force inverse ray shooting algorithm, `GPU-D`, is used to simulate microlensing at the three cusp image components of B1422+231 [74–76]. Such ray tracing simulations have traditionally been used to produce magnification maps and light curves for a source lensed by a random field of stars. The total surface mass density κ has a smooth component represented by κ_s and a compact object component κ_c consisting of point masses with $\kappa = \kappa_s + \kappa_c$. Following Vernardos and Fluke [76], we introduce a smooth matter fraction

$$f_s = \frac{\kappa_s}{\kappa}. \tag{1}$$

The three image components of B1422+231, namely, A, B, and C, are simulated separately with the same smooth matter fraction f_s, but different surface density κ and shear γ determined by the macromodel for the lens galaxy. Within each simulated area that represents an image component, κ and γ are assumed to be constant. This assumption is valid because the three unresolved image components have small angular sizes. The variation of κ and γ within each image component is negligible compared to the uncertainties of

the macromodel. For every image component, the differences between the κ and γ values predicted by different best-fit macromodels in the literature are much larger than their variations within the image component (e.g., [58,77]). The exact κ and γ values from the macromodel are not important, because here we are more interested in the scatter of magnification due to PBH microlensing rather than the exact magnification. To also account for magnification uncertainties from the macromodel, PBH microlensing simulations have to be performed for all the macromodels sampled during lens modeling, which is outside the scope of this study. We choose to adopt the (κ, γ) values at A (0.38, 0.473), B (0.492, 0.628), and C (0.365, 0.378) from Schechter et al. [58] for our simulations, which have been used for stellar microlensing simulations. Our best-fit 'SIE ($\bar{S}_v$)' model predicts similar (κ, γ) values. We assume that the fraction of matter in dark matter is equal to $\Omega_{DM}/\Omega_m = 0.842$ [61] and that smooth matter consists of non-PBH dark matter and baryonic matter. Our simulations explored the scenarios where the fraction of dark matter in PBHs, f_{PBH}, was 10% and 50%. The PBH surface density κ_{PBH} is given by

$$\kappa_{PBH} = f_{PBH}\frac{\Omega_{DM}}{\Omega_m}. \tag{2}$$

The number of microlenses (i.e., PBHs), N_{PBH}, is

$$N_{PBH} = \frac{\kappa_{PBH}A}{\pi\langle M\rangle}, \tag{3}$$

where A is the area where PBHs are randomly distributed and $\langle M\rangle$ is the mean mass of the PBHs following a power law mass function given below with a mass function exponent $\gamma \in (-1, +1)$ [78],

$$\psi(M) \propto M^{\alpha} = M^{\gamma-1} \quad (M_{min} < M < M_{max}). \tag{4}$$

The mass of a PBH, continuous random variable M, satisfying the above mass function can be mapped to a continuous uniform distribution $\mathcal{U}(0,1)$

$$M \sim \left[\left(M_{min}^{\alpha+1} - M_{max}^{\alpha+1}\right)\mathcal{U}(0,1) + M_{max}^{\alpha+1}\right]^{\frac{1}{\alpha+1}}. \tag{5}$$

The two extreme cases where the power law mass function exponent $\gamma = -1$ and $+1$ were explored in our simulations. We generated N_{PBH} random PBH masses and uniformly distributed them in an circular region with area A in the lens plane. This circular region was larger than the area in which light rays were shot. To minimize edge effects, a smaller area within the actual area where light rays were traced was used for estimating the magnification probability distribution. The chosen area must be at least a few times the size of the source in order for the magnification map produced to contain a large enough statistical sample of random source positions on the map. Figure 5 shows an example magnification map of image component B of B1422+231 after convolution with our best-fit source Sérsic profile in Table 3. Image components with larger surface density have more densely populated PBHs. The large-scale horizontal patterns reflect the shear direction. High resolution magnification maps showing individual caustics are useful for simulating microlensing light curves for a source size comparable to the Einstein radius of the microlenses. However, for the purpose of finding the magnification of a source much larger than the average PBH Einstein radius, the PBH caustics do not need be resolved. Our simulations produced low resolution magnification maps that may contain multiple PBHs per pixel. For each f_{PBH} and γ combination, 25 independent 2000×2000 pixels magnification maps were produced. The width of each pixel is equivalent to 3.6 to 26.5 times of the Einstein radius of the average PBH mass, depending on f_{PBH} and γ. The deflection due to each PBH was still solved exactly. Because it was not necessary to resolve the caustics, the number of light rays needed was drastically decreased, averaging 153.33 light rays per pixel. This significantly reduced the computational cost. To calculate the magnifications of A, B and C at 233 GHz, we convolved the magnification

maps with the Sérsic profile in our best-fit source model in Table 3, where the source major axis $a_s = 9.03$ mas. A smaller source size would allow larger fluctuations in the magnification probability distribution, hence a higher probability for flux density ratio anomaly. Fast Fourier transform implemented in `Astropy` [79,80] with periodic boundaries that wrap around the magnification map was used for convolution. Varying the source position angle has an negligible effect on the magnification probability distribution. Random magnification map pixels are drawn at least 4×10^6 times for image A, B, and C to calculate the their ratios. The ratios are binned into bin width of 0.001 to produce the probability distribution functions plotted in Figure 6.

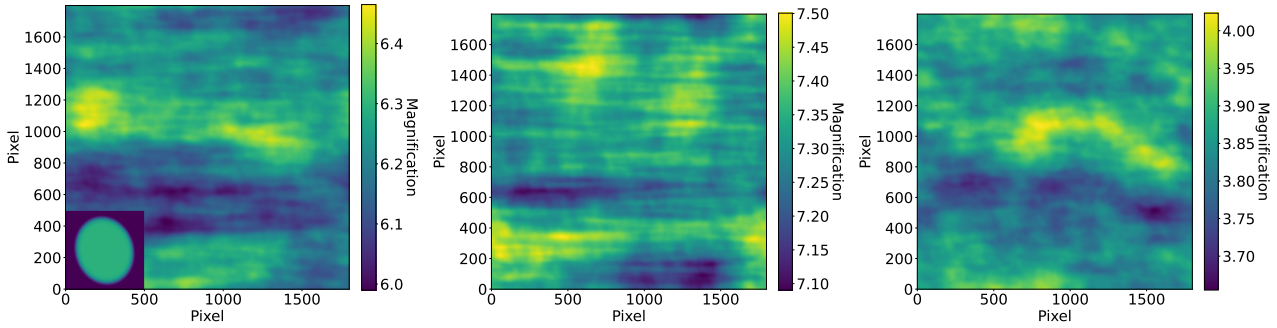


Figure 5. Representative magnification maps for image A, B, and C with $f_{PBH} = 0.5$ and $\gamma = -1$ after convolution with our best-fit Sérsic profile in Table 3. The shape of the source Sérsic profile is illustrated in the bottom left corner.

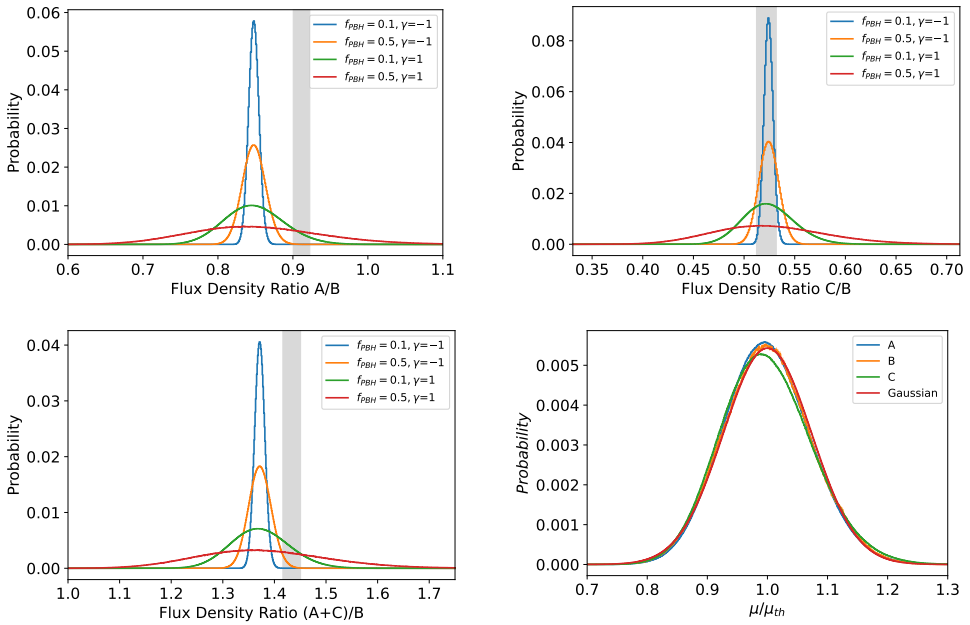


Figure 6. Probability distribution function of flux density ratio A/B (**upper left**), C/B (**upper right**), and (A+C)/B (**lower left**) from PBH microlensing simulations, where f_{PBH} is the fraction of dark matter in PBHs. γ is the power law index of the PBH mass function as defined in Equation (4). The gray color bands show our measured flux density ratios within uncertainties from Table 1. The (**lower right**) panel shows the probability distribution functions of image components' magnification when $f_{PBH} = 0.5$ and $\gamma = 1$, normalized by their respective theoretical magnification predicted by the macromodel. A Gaussian distribution is plotted for comparison. All plotted distributions are histograms with the same bin width 0.001.

5. Simulation Results and Discussion

Figure 6 shows the probability distribution function of the flux density ratios and the magnification probability distributions of image component A, B, and C as functions of the PBH dark matter fraction, f_{PBH}, and the power law index γ of the PBH mass function. We find that for our assumed source major axis of 9.03 mas, the probability distribution function of the flux density ratio (A+C)/B and the magnification probability distributions of the three cusp image components are all well-described by Gaussian distributions. This is in contrast to the asymmetric multi-modal distribution functions of magnification for small source sizes [40,41,58]. Because the assumed source size at 233 GHz is much larger than the Einstein radius of an average PBH, the large fluctuations of magnification probability distribution as the source crosses the caustics are essentially removed when convoluted with the source. Nonetheless, the widths of the probability distribution functions shown in Figure 6 indicate that there is a still non-negligible scatter in magnifications and flux density ratios caused by the microlensing of PBH dark matter. Table 4 lists the *p*-values and confidence intervals of flux density ratio found by our simulations.

We find that a larger fraction of PBH dark matter, f_{PBH}, or a larger power index γ for the PBH mass function both noticeably widens the probability distribution function of the flux density ratios and the magnification probability distributions. With a power law index $\gamma = -1$, the number of PBHs sharply declines as a function of PBH mass. With a power law index $\gamma = 1$, the number of PBHs is approximately constant in each mass bin in the specified mass range 10–1000$M_\odot$. The difference in the power law index γ most directly affects the average PBH mass. The number density of PBHs is proportional to the fraction of PBH dark matter. The lower right panel of Figure 6 shows that for given f_{PBH} and γ, the probability distributions of magnifications normalized by macromodel predicted magnification (μ/μ_{th}) are very close to Gaussian distribution and they does not depend on the surface mass density or shear. More clumpy dark matter, either due to a higher fraction of PBH dark matter or fewer but more massive PBHs, increases the probability of the flux density ratio anomaly. The scatters of flux density ratios and magnifications in Figure 6 are conservative, because stellar populations are considered part of the smooth matter and any scatter produced by stellar microlensing is ignored. Figure 6 shows that a change in the PBH mass function alters the probability of having a large flux density ratio anomaly more significantly than a change of PBH dark matter fraction from 10% to 50%. Without the inclusion of a massive DMS, PBH dark matter between 10–1000$M_\odot$ with a flat mass function alone can produce the observed flux density ratio anomaly. This highlights the need to include the effects of PBH dark matter when considering the causes of flux density ratio anomalies of multiply imaged strong lenses.

Assuming PBH dark matter is the only cause for the flux density ratio anomaly of B1422+231 in our ALMA observation, our simulations show that the probability of observing a flux density ratio (A+C)/B > 1.434 is 31.54% if 50% dark matter is 10–1000$M_\odot$ PBHs with a flat mass function (power law index $\gamma = +1$), and 14.25% if 10% dark matter is 10–1000$M_\odot$ PBHs with a flat mass function (see Table 4). The cases where the PBH mass function is highly skewed towards low masses (power law index $\gamma = -1$) have negligibly small probabilities, regardless of the PBH dark matter fraction. Carr et al. [78] claims that any power law indexγ outside $(-1, +1)$ is not permitted. The logarithmic PBH mass function proposed by Carr et al. [78] also highly skews towards low mass PBHs, so the probabilities assuming a logarithmic PBH mass function should be similarly small compared to those from the power law when $\gamma = -1$. Hence, if PBH dark matter has a mass function highly skewed towards low masses, its contribution to the flux density ratio anomaly should be extremely small even if a significant fraction of dark matter is PBHs. Recent constraints on f_{PBH} allow 100% dark matter being PBHs in the intermediate mass range $10M_\odot < M < 10^3 M_\odot$ [13]. However, more updated constraints suggest that the fraction of PBH dark matter in this mass range is very small, while PBHs below $10^{-10}M_\odot$ may still make up the majority of dark matter [15]. Such low mass PBHs can be treated as smooth matter microlensing simulations. Given that the *p*-values are small for f_{PBH}, it

is very unlikely that PBH dark matter is the only cause for our measured anomalous flux density ratio if $f_{PBH} < 0.1$.

Table 4. *p*-value and Confidence Interval (CI) of the probability distribution of flux density ratios plotted in Figure 6. The *p*-values represent the cumulative probabilities of flux density ratio deviating away from the peak of the distribution more than the values measured by ALMA in Table 1. The confidence interval $z\sigma$ is the proportion of flux density ratios that lie within the smallest symmetric interval $(-z\sigma, +z\sigma)$ that includes the value measured by ALMA in Table 1, assuming a Gaussian distribution with standard deviation σ.

Flux	$f_{PBH} = 0.1$				$f_{PBH} = 0.5$			
Density	$\gamma = -1$		$\gamma = +1$		$\gamma = -1$		$\gamma = +1$	
Ratio	***p*-Value**	**CI**	***p*-Value**	**CI**	***p*-Value**	**CI**	***p*-Value**	**CI**
A/B	0	-	0.0627	1.5322σ	4.373×10^{-5}	3.9230σ	0.2414	0.7017σ
C/B	0.3579	0.3640σ	0.4829	0.04276σ	0.4250	0.1891σ	0.4936	0.01612σ
(A+C)/B	2.000×10^{-8}	5.4909σ	0.1425	1.0691σ	0.002989	2.7490σ	0.3154	0.4806σ

The *p*-values are expected to be higher if there is PBH dark matter outside the 10–1000$M_\odot$ mass range. An additional fraction of PBH dark matter from other mass ranges will result in more microlensing events and widen the probability distributions of the flux density ratios. Treating stars as microlenses instead of a smooth mass component will have a similar effect. In our simulations, stars in the mass range of 10–1000$M_\odot$ are part of the smooth baryonic matter surface density. Therefore, our statistics in Table 4 are conservative estimates of the effects of PBH dark matter on flux density ratios.

DMSs are likely a major contributor to the flux density ratio anomaly of B1422+231 according to previous studies [29,44,73]. Their models add a DMS modeled by a singular isothermal sphere to the macrolens model near image A. In our simulations, we evaluate PBH dark matter as the only cause for the flux density ratio anomaly in B1422+231, to assess the magnitude of this effect. We find that PBH dark matter is a plausible contributor to the flux density ratio anomaly. It is possible that the primary cause for the flux density ratio anomaly in B1422+231 is a DMS and the secondary cause is PBH dark matter. To more conclusively disentangle of the effects of PBH dark matter from DMS, more comprehensive mass models for multi-frequency observations, including low mass perturbers in a wide mass range such as DMs, IMBHs and stars, need to be compared. One key difference between DMS and PBH in causing flux density ratio anomalies is that PBHs as a fraction of dark matter affect all the image components, whereas usually one DMS affects one image component at a time. In principle, there are many low-mass DMSs, but their number density is still much lower than that of PBHs. One can potentially distinguish DMS-caused flux density ratio anomaly from PBHs by checking if only one of the image components has a anomalous flux density.

The biggest uncertainty in constraining the fraction of dark matter in PBHs is the unknown PBH mass function. The uncertainties from the smooth mass model and any massive DMS are the main source of systematic errors of the flux density ratio probability distribution functions. This study focuses on testing the consistency between the mm wave observation and the specific scenario of PBH microlensing in addition to a smooth lens model. It does not consider the scenario of PBH microlensing in the presence of DMSs in the lens halo and line-of-sight substructures, and is thus an upper limit on PBH contributions. Incorporating the results of an ensemble of microlensing simulations with varied PBH mass functions into a full Bayesian analysis of a lens model including a smooth halo component, DMSs, and PBHs has the potential to provide constraints on PBH dark matter fraction and mass function (e.g., [45]). Quadruply lensed compact mm bright quasars with larger flux density ratio anomalies than B1422+231 will give tighter constraints on PBH dark matter.

6. Conclusions

The mass distribution in the foreground lens galaxy of multiply imaged strong gravitational lenses are often not well described by simple smooth lens models. Quadruple lenses such as B1422+231 show flux density ratio anomalies in multi-frequency observations. In radio wave bands, the flux density ratio anomaly is caused by DMSs. We argue that PBH dark matter can be the cause of flux density ratio anomalies in the mm-wave band. In addition to DMSs, PBH dark matter may also be a secondary contributor to the flux density ratio anomaly. In optical and X-ray bands, stellar microlensing is the primary cause for flux density ratio anomaly, but both DMSs and PBH dark matter should be taken into account for lens modeling.

We present the first continuum imaging of B1422+231 using ALMA at 233 GHz. Four unresolved point sources are detected with a total continuum flux density of 6.305 ± 0.082 mJy. The detected compact emission is consistent with the spectral energy distribution of synchrotron emission from the quasar's AGN with almost no thermal dust emission. The flux density ratio (A + B)/C is measured to be 1.434 ± 0.017, consistent with the measurements in radio and mid-infrared frequencies. The smooth lens model is not well constrained by the visibility data directly. Our lens models from mm-wave image plane modeling are similar to those from narrow-line [O III] [29]. Assuming a Sérsic source profile, the source major axis is estimated to be $9.03^{+0.15}_{-0.12}$ mas, corresponding to 66.9 pc at the redshift of this source, similar to the intrinsic [O III] size [29]. Because the source structure is not well resolved, we only consider this source size to be an upper limit.

Our ray tracing microlensing simulations of the three cusp image components show that PBHs in the intermediate mass range $10M_{\odot} < M < 10^3 M_{\odot}$ as a fraction of dark matter can produce flux density ratio anomalies. The magnification probability distribution of image components are well described by Gaussian distributions. A larger fraction of dark matter in PBHs and a less negative power law index for the PBH mass function can both increase the probability of flux density ratio anomaly. Assuming PBHs are the only cause of flux density ratio anomaly for B1422+231, we determine an upper limit to the probability of $(A+C)/B > 1.434$ to be 31.54% for up to 50% dark matter being PBHs, and 14.25% for up to 10% dark matter being PBHs. Our measured flux density ratio (A + B)/C = 1.434 is within 0.4806σ confidence interval of the prediction for 50% dark matter in PBHs with a flat mass function. PBHs with a highly skewed mass function towards low masses has very low probability of being the only cause for the observed flux density ratio anomaly. Simulations with a wide range of PBH dark matter fractions and mass functions are needed to obtain an upper limit for PBH dark matter and compare with limits from Bayesian inference. This is the first study that quantifies the effects of PBHs on the flux density ratio anomaly in mm-wave bands. Our analysis places new constraints on the fraction of PBH dark matter and the PBH mass function using a quadruple lens with flux density ratio anomaly and ray tracing simulations.

Author Contributions: Conceptualization, D.W. and A.J.K.; methodology, D.W.; software, D.W.; validation, D.W.; formal analysis, D.W.; investigation, D.W.; resources, A.J.K.; data curation, D.W.; writing—original draft, D.W.; writing—review and editing, D.W. and A.J.K.; visualization, D.W.; supervision, A.J.K.; project administration, A.J.K.; funding acquisition, A.J.K. All authors have read and agreed to the published version of the manuscript.

Funding: Support for this work was provided by the NSF through award SOSPA6-019 from the NRAO. The National Radio Astronomy Observatory is a facility of the National Science Foundation operated under cooperative agreement by Associated Universities, Inc. This research is part of the Blue Waters sustained-petascale computing project, which is supported by the National Science Foundation (awards OCI-0725070 and ACI-1238993) the State of Illinois, and as of December, 2019, the National Geospatial-Intelligence Agency. Blue Waters is a joint effort of the University of Illinois at Urbana-Champaign and its National Center for Supercomputing Applications. DW acknowledges support from The Netherlands Organization for Scientific Research (NWO) (Project No. 629.001.023) and the Chinese Academy of Sciences (CAS) (Project No. 114A11KYSB20170054).

Data Availability Statement: This paper makes use of the following ALMA data: ADS/JAO.ALMA#2018.1.00915.S. ALMA is a partnership of ESO (representing its member states), NSF (USA) and NINS (Japan), together with NRC (Canada), MOST and ASIAA (Taiwan), and KASI (Republic of Korea), in cooperation with the Republic of Chile. The Joint ALMA Observatory is operated by ESO, AUI/NRAO and NAOJ.

Acknowledgments: We thank John P. McKean for insightful discussions about the interpretation of the ALMA observation and Garrett K. Keating for sharing the flux density measurement of B1422+231 from the Submillimeter Array. D.W. thanks the Center for Information Technology of the University of Groningen for their support and for providing access to the Peregrine high performance computing cluster.

Conflicts of Interest: The authors declare no conflicts of interest.

Abbreviations

The following abbreviations are used in this manuscript:

ALMA	Atacama Large Millimeter Array
PBH	Primordial black hole
DMS	Dark matter substructure
IMBH	Intermediate-mass black hole
CASA	Common Astronomy Software Applications
AGN	Active galactic nucleus

References

1. Bird, S.; Cholis, I.; Muñoz, J.B.; Ali-Haïmoud, Y.; Kamionkowski, M.; Kovetz, E.D.; Raccanelli, A.; Riess, A.G. Did LIGO Detect Dark Matter? *Phys. Rev. Lett.* **2016**, *116*, 201301. [CrossRef] [PubMed]
2. Carr, B.; Kühnel, F.; Sandstad, M. Primordial black holes as dark matter. *Phys. Rev. D* **2016**, *94*, 083504. [CrossRef]
3. Abbott, B.P.; Abbott, R.; Abbott, T.D.; Abernathy, M.R.; Acernese, F.; Ackley, K.; Adams, C.; Adams, T.; Addesso, P.; Adhikari, R.X.; et al. Observation of Gravitational Waves from a Binary Black Hole Merger. *Phys. Rev. Lett.* **2016**, *116*, 061102. [CrossRef] [PubMed]
4. Abbott, B.P.; Abbott, R.; Abbott, T.D.; Abraham, S.; Acernese, F.; Ackley, K.; Adams, C.; Adhikari, R.X.; Adya, V.B.; Affeldt, C.; et al. Binary Black Hole Population Properties Inferred from the First and Second Observing Runs of Advanced LIGO and Advanced Virgo. *Astrophys. J. Lett.* **2019**, *882*, L24. [CrossRef]
5. Green, A.M. Microlensing and dynamical constraints on primordial black hole dark matter with an extended mass function. *Phys. Rev. D* **2016**, *94*, 063530. [CrossRef]
6. Mediavilla, E.; Jiménez-Vicente, J.; Muñoz, J.A.; Vives-Arias, H.; Calderón-Infante, J. Limits on the Mass and Abundance of Primordial Black Holes from Quasar Gravitational Microlensing. *Astrophys. J. Lett.* **2017**, *836*, L18. [CrossRef]
7. Brandt, T.D. Constraints on MACHO Dark Matter from Compact Stellar Systems in Ultra-faint Dwarf Galaxies. *Astrophys. J. Lett.* **2016**, *824*, L31. [CrossRef]
8. Koushiappas, S.M.; Loeb, A. Dynamics of Dwarf Galaxies Disfavor Stellar-Mass Black Holes as Dark Matter. *Phys. Rev. Lett.* **2017**, *119*, 041102. [CrossRef]
9. Zhu, Q.; Vasiliev, E.; Li, Y.; Jing, Y. Primordial black holes as dark matter: constraints from compact ultra-faint dwarfs. *Mon. Not. R. Astron. Soc.* **2018**, *476*, 2–11. [CrossRef]
10. Quinn, D.P.; Wilkinson, M.I.; Irwin, M.J.; Marshall, J.; Koch, A.; Belokurov, V. On the reported death of the MACHO era. *Mon. Not. R. Astron. Soc.* **2009**, *396*, L11–L15. [CrossRef]
11. Yoo, J.; Chanamé, J.; Gould, A. The End of the MACHO Era: Limits on Halo Dark Matter from Stellar Halo Wide Binaries. *Astrophys. J.* **2004**, *601*, 311–318. [CrossRef]
12. Abbott, R.; Abbott, T.D.; Abraham, S.; Acernese, F.; Ackley, K.; Adams, C.; Adhikari, R.X.; Adya, V.B.; Affeldt, C.; Agathos, M.; et al. GW190521: A Binary Black Hole Merger with a Total Mass of 150 $M_{\odot}$. *Phys. Rev. Lett.* **2020**, *125*, 101102. [CrossRef] [PubMed]
13. Carr, B.; Kühnel, F. Primordial Black Holes as Dark Matter: Recent Developments. *Annu. Rev. Nucl. Part. Sci.* **2020**, *70*, 355–394. [CrossRef]
14. Carr, B.; Clesse, S.; García-Bellido, J.; Kühnel, F. Cosmic conundra explained by thermal history and primordial black holes. *Phys. Dark Univ.* **2021**, *31*, 100755. [CrossRef]
15. Carr, B.; Kohri, K.; Sendouda, Y.; Yokoyama, J. Constraints on primordial black holes. *Rep. Prog. Phys.* **2021**, *84*, 116902. [CrossRef]
16. Miller, M.C.; Colbert, E.J.M. Intermediate-Mass Black Holes. *Int. J. Mod. Phys. D* **2004**, *13*, 1–64. [CrossRef]
17. Clowe, D.; Bradač, M.; Gonzalez, A.H.; Markevitch, M.; Randall, S.W.; Jones, C.; Zaritsky, D. A Direct Empirical Proof of the Existence of Dark Matter. *Astrophys. J. Lett.* **2006**, *648*, L109–L113. [CrossRef]

18. Schneider, P.; Ehlers, J.; Falco, E.E. *Gravitational Lenses*; Springer: New York, NY, USA, 1992. [CrossRef]
19. Kochanek, C.S. Part 2: Strong gravitational lensing. In *Saas-Fee Advanced Course 33: Gravitational Lensing: Strong, Weak and Micro*; Meylan, G., Jetzer, P., North, P., Schneider, P., Kochanek, C.S., Wambsganss, J., Eds.; Springer: Berlin/Heidelberg, Germany, 2006; pp. 91–268.
20. Klypin, A.; Kravtsov, A.V.; Valenzuela, O.; Prada, F. Where Are the Missing Galactic Satellites? *Astrophys. J.* **1999**, *522*, 82–92. [CrossRef]
21. Moore, B.; Ghigna, S.; Governato, F.; Lake, G.; Quinn, T.; Stadel, J.; Tozzi, P. Dark Matter Substructure within Galactic Halos. *Astrophys. J. Lett.* **1999**, *524*, L19–L22. [CrossRef]
22. Bullock, J.S. Notes on the Missing Satellites Problem. *arXiv* **2010**, arXiv:1009.4505.
23. Bullock, J.S.; Boylan-Kolchin, M. Small-Scale Challenges to the ΛCDM Paradigm. *Annu. Rev. Astron. Astrophys.* **2017**, *55*, 343–387. [CrossRef]
24. Nadler, E.O.; Drlica-Wagner, A.; Bechtol, K.; Mau, S.; Wechsler, R.H.; Gluscevic, V.; Boddy, K.; Pace, A.B.; Li, T.S.; McNanna, M.; et al. Constraints on Dark Matter Properties from Observations of Milky Way Satellite Galaxies. *Phys. Rev. Lett.* **2021**, *126*, 091101. [CrossRef] [PubMed]
25. Vegetti, S.; Koopmans, L.V.E. Bayesian strong gravitational-lens modelling on adaptive grids: objective detection of mass substructure in Galaxies. *Mon. Not. R. Astron. Soc.* **2009**, *392*, 945–963. [CrossRef]
26. Vegetti, S.; Lagattuta, D.J.; McKean, J.P.; Auger, M.W.; Fassnacht, C.D.; Koopmans, L.V.E. Gravitational detection of a low-mass dark satellite galaxy at cosmological distance. *Nature* **2012**, *481*, 341–343. [CrossRef] [PubMed]
27. Hezaveh, Y.; Dalal, N.; Holder, G.; Kuhlen, M.; Marrone, D.; Murray, N.; Vieira, J. Dark Matter Substructure Detection Using Spatially Resolved Spectroscopy of Lensed Dusty Galaxies. *Astrophys. J.* **2013**, *767*, 9. [CrossRef]
28. MacLeod, C.L.; Jones, R.; Agol, E.; Kochanek, C.S. Detection of Substructure in the Gravitationally Lensed Quasar MG0414+0534 Using Mid-infrared and Radio VLBI Observations. *Astrophys. J.* **2013**, *773*, 35. [CrossRef]
29. Nierenberg, A.M.; Treu, T.; Wright, S.A.; Fassnacht, C.D.; Auger, M.W. Detection of substructure with adaptive optics integral field spectroscopy of the gravitational lens B1422+231. *Mon. Not. R. Astron. Soc.* **2014**, *442*, 2434–2445. [CrossRef]
30. Hezaveh, Y.D.; Dalal, N.; Marrone, D.P.; Mao, Y.Y.; Morningstar, W.; Wen, D.; Blandford, R.D.; Carlstrom, J.E.; Fassnacht, C.D.; Holder, G.P.; et al. Detection of Lensing Substructure Using ALMA Observations of the Dusty Galaxy SDP.81. *Astrophys. J.* **2016**, *823*, 37. [CrossRef]
31. Hezaveh, Y.; Dalal, N.; Holder, G.; Kisner, T.; Kuhlen, M.; Perreault Levasseur, L. Measuring the power spectrum of dark matter substructure using strong gravitational lensing. *J. Cosmol. Astro-Part. Phys.* **2016**, *2016*, 048. [CrossRef]
32. Cyr-Racine, F.Y.; Keeton, C.R.; Moustakas, L.A. Beyond subhalos: Probing the collective effect of the Universe's small-scale structure with gravitational lensing. *Phys. Rev. D* **2019**, *100*, 023013. [CrossRef]
33. Gilman, D.; Birrer, S.; Nierenberg, A.; Treu, T.; Du, X.; Benson, A. Warm dark matter chills out: Constraints on the halo mass function and the free-streaming length of dark matter with eight quadruple-image strong gravitational lenses. *Mon. Not. R. Astron. Soc.* **2020**, *491*, 6077–6101. [CrossRef]
34. Ostdiek, B.; Diaz Rivero, A.; Dvorkin, C. Extracting the Subhalo Mass Function from Strong Lens Images with Image Segmentation. *Astrophys. J.* **2022**, *927*, 83. [CrossRef]
35. Dalal, N.; Kochanek, C.S. Direct Detection of Cold Dark Matter Substructure. *Astrophys. J.* **2002**, *572*, 25–33. [CrossRef]
36. Chen, J.; Kravtsov, A.V.; Keeton, C.R. Lensing Optical Depths for Substructure and Isolated Dark Matter Halos. *Astrophys. J.* **2003**, *592*, 24–31. [CrossRef]
37. Metcalf, R.B. The Importance of Intergalactic Structure to Gravitationally Lensed Quasars. *Astrophys. J.* **2005**, *629*, 673–679. [CrossRef]
38. Wambsganss, J.; Bode, P.; Ostriker, J.P. Gravitational Lensing in a Concordance ΛCDM Universe: The Importance of Secondary Matter along the Line of Sight. *Astrophys. J. Lett.* **2005**, *635*, L1–L4. [CrossRef]
39. Xu, D.D.; Mao, S.; Cooper, A.P.; Gao, L.; Frenk, C.S.; Angulo, R.E.; Helly, J. On the effects of line-of-sight structures on lensing flux-ratio anomalies in a ΛCDM universe. *Mon. Not. R. Astron. Soc.* **2012**, *421*, 2553–2567. [CrossRef]
40. Schechter, P.L.; Wambsganss, J. Quasar Microlensing at High Magnification and the Role of Dark Matter: Enhanced Fluctuations and Suppressed Saddle Points. *Astrophys. J.* **2002**, *580*, 685–695. [CrossRef]
41. Schechter, P.L.; Wambsganss, J.; Lewis, G.F. Qualitative Aspects of Quasar Microlensing with Two Mass Components: Magnification Patterns and Probability Distributions. *Astrophys. J.* **2004**, *613*, 77–85. [CrossRef]
42. Wambsganss, J. Part 4: Gravitational microlensing. In *Saas-Fee Advanced Course 33: Gravitational Lensing: Strong, Weak and Micro*; Meylan, G., Jetzer, P., North, P., Schneider, P., Kochanek, C.S., Wambsganss, J., Eds.; Springer: Berlin/Heidelberg, Germany, 2006; pp. 453–540.
43. Barvainis, R.; Ivison, R. A Submillimeter Survey of Gravitationally Lensed Quasars. *Astrophys. J.* **2002**, *571*, 712–720. [CrossRef]
44. Xu, D.; Sluse, D.; Gao, L.; Wang, J.; Frenk, C.; Mao, S.; Schneider, P.; Springel, V. How well can cold dark matter substructures account for the observed radio flux-ratio anomalies. *Mon. Not. R. Astron. Soc.* **2015**, *447*, 3189–3206. [CrossRef]
45. Dike, V.; Gilman, D.; Treu, T. Strong lensing constraints on primordial black holes as a dark matter candidate. *Mon. Not. R. Astron. Soc.* **2023**, *522*, 5434–5441. [CrossRef]

46. McMullin, J.P.; Waters, B.; Schiebel, D.; Young, W.; Golap, K. CASA Architecture and Applications. In *Astronomical Data Analysis Software and Systems XVI*; Shaw, R.A., Hill, F., Bell, D.J., Eds.; Astronomical Society of the Pacific Conference Series; ASP: San Francisco, CA, USA, 2007; Volume 376, p. 127.
47. Keating, G.K. (Center for Astrophysics, Harvard & Smithsonian, Cambridge, MA, USA). Private Communication, 2018.
48. Tinti, S.; Dallacasa, D.; de Zotti, G.; Celotti, A.; Stanghellini, C. High Frequency Peakers: Young radio sources or flaring blazars? *Astron. Astrophys.* **2005**, *432*, 31–43. .:20041620 [CrossRef]
49. Stacey, H.R.; McKean, J.P.; Robertson, N.C.; Ivison, R.J.; Isaak, K.G.; Schleicher, D.R.G.; van der Werf, P.P.; Baan, W.A.; Berciano Alba, A.; Garrett, M.A.; et al. Gravitational lensing reveals extreme dust-obscured star formation in quasar host galaxies. *Mon. Not. R. Astron. Soc.* **2018**, *476*, 5075–5114. [CrossRef]
50. Urry, C.M.; Padovani, P. Unified Schemes for Radio-Loud Active Galactic Nuclei. *Publ. Astron. Soc. Pac.* **1995**, *107*, 803. [CrossRef]
51. Patnaik, A.R.; Browne, I.W.A.; Walsh, D.; Chaffee, F.H.; Foltz, C.B. B 1422+231: A new gravitationally lensed system at Z = 3.62. *Mon. Not. R. Astron. Soc.* **1992**, *259*, 1P–4P. [CrossRef]
52. Lawrence, C.R.; Neugebauer, G.; Weir, N.; Matthews, K.; Patnaik, A.R. Infrared observations of the gravitational lens system B 1422+231. *Mon. Not. R. Astron. Soc.* **1992**, *259*, 5P–7P. [CrossRef]
53. Impey, C.D.; Foltz, C.B.; Petry, C.E.; Browne, I.W.A.; Patnaik, A.R. Hubble Space Telescope Observations of the Gravitational Lens System B1422+231. *Astrophys. J. Lett.* **1996**, *462*, L53. [CrossRef]
54. Condon, J.J. Errors in Elliptical Gaussian Fits. *Publ. Astron. Soc. Pac.* **1997**, *109*, 166–172. [CrossRef]
55. Chiba, M.; Minezaki, T.; Kashikawa, N.; Kataza, H.; Inoue, K.T. Subaru Mid-Infrared Imaging of the Quadruple Lenses PG 1115+080 and B1422+231: Limits on Substructure Lensing. *Astrophys. J.* **2005**, *627*, 53–61. [CrossRef]
56. Sluse, D.; Chantry, V.; Magain, P.; Courbin, F.; Meylan, G. COSMOGRAIL: The COSmological MOnitoring of GRAvItational Lenses. X. Modeling based on high-precision astrometry of a sample of 25 lensed quasars: Consequences for ellipticity, shear, and astrometric anomalies. *Astron. Astrophys.* **2012**, *538*, A99. [CrossRef]
57. Pooley, D.; Rappaport, S.; Blackburne, J.A.; Schechter, P.L.; Wambsganss, J. X-Ray and Optical Flux Ratio Anomalies in Quadruply Lensed Quasars. II. Mapping the Dark Matter Content in Elliptical Galaxies. *Astrophys. J.* **2012**, *744*, 111. [CrossRef]
58. Schechter, P.L.; Pooley, D.; Blackburne, J.A.; Wambsganss, J. A Calibration of the Stellar Mass Fundamental Plane at z $\sim$0.5 Using the Micro-lensing-induced Flux Ratio Anomalies of Macro-lensed Quasars. *Astrophys. J.* **2014**, *793*, 96. [CrossRef]
59. Kundic, T.; Hogg, D.W.; Blandford, R.D.; Cohen, J.G.; Lubin, L.M.; Larkin, J.E. The External Shear Acting on Gravitational Lens B1422+231. *Astron. J.* **1997**, *114*, 2276. [CrossRef]
60. Tonry, J.L. Redshifts of the Gravitational Lenses B1422+231 and PG 1115+080. *Astron. J.* **1998**, *115*, 1–5. [CrossRef]
61. Ade, P.A.R. et al. [Planck Collaboration]. Planck 2015 results. XIII. Cosmological parameters. *Astron. Astrophys.* **2016**, *594*, A13. [CrossRef]
62. Oguri, M. The Mass Distribution of SDSS J1004+4112 Revisited. *Publ. Astron. Soc. Jpn.* **2010**, *62*, 1017. [CrossRef]
63. Hezaveh, Y.D.; Marrone, D.P.; Fassnacht, C.D.; Spilker, J.S.; Vieira, J.D.; Aguirre, J.E.; Aird, K.A.; Aravena, M.; Ashby, M.L.N.; Bayliss, M.; et al. ALMA Observations of SPT-discovered, Strongly Lensed, Dusty, Star-forming Galaxies. *Astrophys. J.* **2013**, *767*, 132. [CrossRef]
64. Spilker, J.S.; Marrone, D.P.; Aravena, M.; Béthermin, M.; Bothwell, M.S.; Carlstrom, J.E.; Chapman, S.C.; Crawford, T.M.; de Breuck, C.; Fassnacht, C.D.; et al. ALMA Imaging and Gravitational Lens Models of South Pole Telescope—Selected Dusty, Star-Forming Galaxies at High Redshifts. *Astrophys. J.* **2016**, *826*, 112. [CrossRef]
65. Sérsic, J.L. Influence of the atmospheric and instrumental dispersion on the brightness distribution in a galaxy. *Bol. Asoc. Argent. Astron. Plata Argent.* **1963**, *6*, 41–43.
66. Feroz, F.; Hobson, M.P. Multimodal nested sampling: An efficient and robust alternative to Markov Chain Monte Carlo methods for astronomical data analyses. *Mon. Not. R. Astron. Soc.* **2008**, *384*, 449–463. [CrossRef]
67. Feroz, F.; Hobson, M.P.; Bridges, M. MULTINEST: An efficient and robust Bayesian inference tool for cosmology and particle physics. *Mon. Not. R. Astron. Soc.* **2009**, *398*, 1601–1614. [CrossRef]
68. Feroz, F.; Hobson, M.P.; Cameron, E.; Pettitt, A.N. Importance Nested Sampling and the MultiNest Algorithm. *Open J. Astrophys.* **2019**, *2*, 10. [CrossRef]
69. Buchner, J.; Georgakakis, A.; Nandra, K.; Hsu, L.; Rangel, C.; Brightman, M.; Merloni, A.; Salvato, M.; Donley, J.; Kocevski, D. X-ray spectral modelling of the AGN obscuring region in the CDFS: Bayesian model selection and catalogue. *Astron. Astrophys.* **2014**, *564*, A125. [CrossRef]
70. Thompson, A.R.; Moran, J.M.; Swenson, G.W., Jr. *Interferometry and Synthesis in Radio Astronomy*, 3rd ed.; Springer: Cham, Switzerland, 2017. [CrossRef]
71. Kormann, R.; Schneider, P.; Bartelmann, M. A gravitational lens model for B1422+231. *Astron. Astrophys.* **1994**, *286*, 357–364.
72. Bradač, M.; Schneider, P.; Steinmetz, M.; Lombardi, M.; King, L.J.; Porcas, R. B1422+231: The influence of mass substructure on strong lensing. *Astron. Astrophys.* **2002**, *388*, 373–382. [CrossRef]
73. Chiba, M. Probing Dark Matter Substructure in Lens Galaxies. *Astrophys. J.* **2002**, *565*, 17–23. [CrossRef]
74. Thompson, A.C.; Fluke, C.J.; Barnes, D.G.; Barsdell, B.R. Teraflop per second gravitational lensing ray-shooting using graphics processing units. *New Astron.* **2010**, *15*, 16–23. [CrossRef]
75. Bate, N.F.; Fluke, C.J.; Barsdell, B.R.; Garsden, H.; Lewis, G.F. Computational advances in gravitational microlensing: A comparison of CPU, GPU, and parallel, large data codes. *New Astron.* **2010**, *15*, 726–734. [CrossRef]

76. Vernardos, G.; Fluke, C.J. Adventures in the microlensing cloud: Large datasets, eResearch tools, and GPUs. *Astron. Comput.* **2014**, *6*, 1–18. [CrossRef]
77. Mediavilla, E.; Muñoz, J.A.; Falco, E.; Motta, V.; Guerras, E.; Canovas, H.; Jean, C.; Oscoz, A.; Mosquera, A.M. Microlensing-based Estimate of the Mass Fraction in Compact Objects in Lens Galaxies. *Astrophys. J.* **2009**, *706*, 1451–1462. [CrossRef]
78. Carr, B.; Raidal, M.; Tenkanen, T.; Vaskonen, V.; Veermäe, H. Primordial black hole constraints for extended mass functions. *Phys. Rev. D* **2017**, *96*, 023514. [CrossRef]
79. Robitaille, T.P. et al. [Astropy Collaboration]. Astropy: A community Python package for astronomy. *Astron. Astrophys.* **2013**, *558*, A33. [CrossRef]
80. Price-Whelan, A.M. et al. [Astropy Collaboration]. The Astropy Project: Building an Open-science Project and Status of the v2.0 Core Package. *Astron. J.* **2018**, *156*, 123. [CrossRef]

Disclaimer/Publisher's Note: The statements, opinions and data contained in all publications are solely those of the individual author(s) and contributor(s) and not of MDPI and/or the editor(s). MDPI and/or the editor(s) disclaim responsibility for any injury to people or property resulting from any ideas, methods, instructions or products referred to in the content.